

A Microstructural Study of Grain Boundary Engineered Alloy 800H

DANIEL J. DRABBLE, CATHERINE M. BISHOP, and MILO V. KRAL

A series of grain boundary engineering (GBE) procedures was performed on samples of 800H, a common iron-nickel base alloy. The effects of varying the GBE parameters (deformation percentage and annealing temperature/time) were examined using electron backscatter diffraction orientation mapping. GBE samples exhibited up to a 70 pct increase in $\Sigma 3^n$ boundary length fraction compared to the as-received condition. The incorporation of these $\Sigma 3^n$ boundaries was also measured using a simplified model of two-dimensional grain boundary transport and its electrical analogy. The results showed that GBE resulted in increased resistance to grain boundary diffusion compared to the as-received condition. The evolution of a GBE microstructure was also studied on a per-cycle basis, and the results are shown to be consistent with previous studies.

DOI: 10.1007/s11661-010-0447-4

© The Minerals, Metals & Materials Society and ASM International 2010

I. INTRODUCTION

GRAIN boundary engineering (GBE) is a relatively new technique for improving the material properties of metals and alloys with low stacking-fault energy. The aim of GBE processing is to manipulate the grain boundary network in order to create greater resistance to grain boundary-influenced damage mechanisms. First proposed in 1984,^[1] many GBE studies have shown success in improving desired properties in face-centered-cubic materials such as nickel alloys, copper, and brass through the use of GBE. A summary of such studies is contained in an overview by Randle.^[2]

GBE has been employed typically to combat the effects of intergranular corrosion,^[3] cracking,^[4] and creep,^[5] although success has also been shown in areas of ductility,^[6] weldability,^[7] and microstructural stability.^[8] In almost all cases, the GBE process itself involves a series of thermomechanical cycles. These cycles typically consist of a deformation step (such as plate rolling), followed by an annealing step, and are normally repeated between 3 and 7 times. The effect of the processing has generally been an increase in the fraction of low- Σ coincidence-site-lattice (CSL) grain boundaries with respect to the fraction of randomly oriented high-angle boundaries (HABs). Early work suggested that these low- Σ grain boundaries (sometimes termed “special boundaries,” although this term has become somewhat ambiguous) have superior properties compared to random HABs due to their potential for structural order in the boundary plane.^[9]

The term “special boundary” generally refers to a boundary classed according to the CSL nomenclature as

having $\Sigma < 29$, where Σ is the reciprocal of the fraction of coincident lattice sites across a grain boundary, should the two grains be theoretically superimposed. Hence, there is some periodicity across the boundary (*i.e.*, it is geometrically “special”), as opposed to a random HAB.

Electron backscattered diffraction (EBSD) is typically employed to identify these low- Σ grain boundaries, and provides a measure of the effectiveness of GBE processing by simple statistics such as the fraction of total grain boundary length identified as low- Σ . EBSD orientation maps are built up by calculating the crystal orientation from diffraction patterns in a defined grid of points on a polished surface. These crystal orientation data are then used to determine grain boundary misorientation for each boundary segment. This misorientation is checked against specific misorientations unique to each Σ value, and thus, a Σ value can be assigned to a grain boundary based on the misorientation between adjoining crystals. However, the CSL model used in EBSD measurements only describes the relative misorientation between two adjacent grains (three parameters) but does not give the orientation of the grain boundary plane itself (two parameters) and so provides an incomplete description of the boundary. In addition, although the link between low- Σ boundaries and improved properties has been suggested on many occasions, recent studies have shown that this is almost certainly an indirect relationship.^[10] A technique has been documented for measuring the five-parameter grain boundary distribution,^[11] based on single section trace analysis. Despite this, the CSL model is still often used, though it is normally in conjunction with other information such as triple point analyses (*e.g.*, Reference 12). The main reason for using the CSL model is convenience, since identification of specific Σ -value grain boundaries by EBSD is fast, accurate, and repeatable.

The $\Sigma 3$ boundary fraction is thought to be the greatest contributor to improved material properties and is the only CSL boundary type shown to have consistently

DANIEL J. DRABBLE, Graduate Student, and CATHERINE M. BISHOP and MILO V. KRAL, Associate Professors, are with the Department of Mechanical Engineering, University of Canterbury, Christchurch 8041, New Zealand. Contact e-mail: milo.kral@canterbury.ac.nz

Manuscript submitted October 18, 2009.

Article published online November 24, 2010

different characteristics to those of random HABs. The coherent annealing twin boundary has $\{1\ 1\ 1\}$ boundary planes and the lowest free volume of the $\Sigma 3$ boundaries.^[13] Also, a linear correlation exists between the energy of a boundary and its free volume.^[14] Other $\Sigma 3$ boundaries, such as the incoherent twin on $\{1\ 1\ 2\}$ planes and other incoherent boundaries including tilt and twist boundaries on low-index planes, have higher energies than the coherent twin, but still are much lower than the average of random HABs. A study by Randle^[10] showed that in pure nickel, those $\Sigma 3$ boundaries considered to be special (classed as symmetrical tilt, twist, or asymmetrical tilt boundaries with one low index plane, as well as those on the 011 zone) comprised over 80 pct of the total number of $\Sigma 3$ s. In fact, recent research^[15] has suggested that the boundaries with special properties are the ones terminated by low-index planes.

Of the other low- Σ boundaries, only the fractions of the $\Sigma 3''$ family ($\Sigma 9$ and $\Sigma 27$) are generally increased by GBE processing. Thus, it is useful to know whether these boundaries also exhibit special properties. Certainly, the $\Sigma 9$ descriptor includes boundary configurations, which are of lower energy than the HAB average.^[13] However, the boundary must again be fully described to calculate this. In the same study mentioned previously,^[10] the proportion of $\Sigma 9$ s with assumed special properties was approximately 60 pct. An investigation using atomic force microscopy combined with EBSD orientation mapping^[16] showed that in a “bamboo-structured” sample of INCONEL* 600, the $\Sigma 9$ and

*INCONEL is a trademark of Special Metals Corporation, New Hartford, NY.

$\Sigma 27$ boundaries generally possessed lower energies than the average of the HABs. A recent study^[17] concluded that the $\Sigma 9$ boundaries are more resistant to corrosion than HABs in sensitized 304 stainless steel sheet. The authors came to the common conclusion that the more a boundary plane deviates from the exact CSL position, the more “normal” (in this case, more susceptible to corrosion) the properties become. In contrast to this, another recent study^[18] using copper showed that $\Sigma 9$ and $\Sigma 27$ boundaries had irrational boundary planes, implying that they had no special properties.

The property improvements, which are achieved *via* GBE, are often attributed to the interruption of the HABs as an interconnected network, through the incorporation of grain boundaries with special properties (*i.e.*, lower diffusivity, higher probability of crack arrest, *etc.*). Attempts have been made to quantify the level of disruption to the HAB network by such means as triple point analysis (*e.g.*, Reference 12) or cluster analysis.^[19,20] In typical triple point analyses, the number of adjoining random (nonspecial) boundaries is counted at each triple point. The effects of GBE are measured by the fractions of triple points at the intersection of two or three special boundaries, which are shown to increase relative to the fractions of those at the intersection of zero or one special boundary. However, triple point

analysis does not quantify the disruption to the random boundary network, since there is no way to distinguish special boundaries that interrupt the random boundary network from those that do not. In cluster analysis, the individual interconnected “clusters” of each boundary type are analyzed and the average “cluster mass” for random boundary clusters is shown to decrease significantly after GBE processing. For example, in as-received René 41**, over 95 pct of the random HABs

**René 41 is a trademark of ATI Properties Inc., Monroe, NC.

were in clusters larger than 500 grain diameters.^[20] This percentage was then reduced to zero in the grain boundary-engineered microstructures, indicating that the percolating network of HABs was disrupted by the GBE process. This method is a much more direct measure of boundary connectivity and has shown some correlation with material properties.^[19] A third method was used by Chen and Schuh,^[21] who analyzed GBE structures as two-dimensional hexagonal diffusion networks. In their analysis, each grain boundary segment was classified according to a binary system as either special or nonspecial, and assigned a diffusivity based on its boundary classification. The geometric network of grain boundaries was then solved using Fick’s first law combined with mass conservation at each junction, and a single “effective grain boundary diffusivity” was extracted. However, the microstructures used in this analysis were simulated, made up of perfect hexagons in a grid pattern where the fraction of special boundaries could be adjusted to simulate various degrees of GBE.

In the present work, a model of grain boundary connectivity is presented, which is similar to the work of Chen and Schuh, but applied to real microstructures, digitized by EBSD analysis. The model also describes a situation of two-dimensional grain boundary diffusion, and an analogous electric circuit model is applied. In the analogous electric circuit, the grain boundaries become a network of resistors of varying resistance, depending on boundary length and character. The aim of this model was to quantify the effect of special boundaries in a real microstructure, based on the actual boundary topology that GBE microstructures exhibit, and to compare this effect between samples of differing thermomechanical history. By modeling the diffusional properties of the microstructure, it is expected that correlations may also be drawn with grain boundary diffusion-based material properties, such as Coble creep rate.

For each sample analyzed in this work, 24 EBSD maps measuring 1×1 mm were examined. The digitized images were used to construct a network of resistors and the effective resistance of the network was calculated. Grain boundaries are interpreted as resistors with a resistivity determined by the grain boundary character. For this model, boundary segments were identified as either special ($\Sigma 3''$) or nonspecial. A study in 2003 of an austenitic Ni-16Cr-9Fe alloy^[22] concluded that, on average, the low- Σ ($\Sigma < 29$) grain boundary diffusion coefficient was approximately 12

times lower than that of the HABs (this low- Σ network consisted primarily of $\Sigma 3$ s, as do the present microstructures). Therefore, in the present analysis, the resistivity ratio of $\rho_{(\Sigma 3n)}/\rho_{(\text{HAB})} = 12$ was also used, although it is recognized that there is potential for further refinement of the model to include information based on boundary type and boundary plane configurations.

The resistance of resistor j is $R_j = l_j \rho_j$, where l_j is the length of the grain boundary segment and ρ_j is the resistivity (either $\rho_{(\Sigma 3n)}$ or $\rho_{(\text{HAB})}$ depending on the grain boundary character). There are a total of n_t nodes in the network where subsets of the m resistors meet. The set of n_t terminating nodes on the left are assigned a voltage V^+ , and the set of n_r terminating nodes on the right are assigned voltage zero. The current in each resistor is determined by solving a set of m linearly independent equations generated from $n = n_t - n_l - n_r$ equations corresponding to Kirchoff's Current Law at each internal node and $m-n$ equations corresponding to Kirchoff's Voltage Law for independent paths across the network from left to right.

The first n equations have the form $\sum_k a_{jk} i_k = 0$ for node j , where $a_{jk} = \pm 1$ for resistors transporting current to or from the node and $a_{jk} = 0$ for all others. The final $m-n$ equations have the form $\sum_k c_{jk} R_k i_k = V^+$, where $c_{jk} = 1$ for resistors in the j th path and $c_{jk} = 0$ for all others. In matrix form, $\mathbf{A}\mathbf{i} = \mathbf{b}$ is solved for \mathbf{i} , where \mathbf{A} is the $m \times m$ matrix of coefficients, \mathbf{i} is the $m \times 1$ vector of currents, and \mathbf{b} is an $m \times 1$ vector.

The effective resistance depends on the grain size in that, as grain size increases, the number of paths decreases and R_{eff} increases. The aim of the following analysis is to isolate the topological effects of GBE by removing the grain size effect. An exact solution for the grain size dependence of the effective resistance can be obtained for a self-similar microstructure.

Consider a network of resistors arranged in a regular hexagonal grid, as shown in Figure 1(a). Compare such a network comprising resistors of unit length to a network comprising the same number of resistors of length x (shown in Figure 1(b)). The ratio of the effective resistances of these two networks is $R_{\text{eff},x}/R_{\text{eff},1} = 1/x$. The relationship can be shown by considering the equations from which the net current is determined. For the first case, $\mathbf{A}\mathbf{i} = \mathbf{b}$ according to the

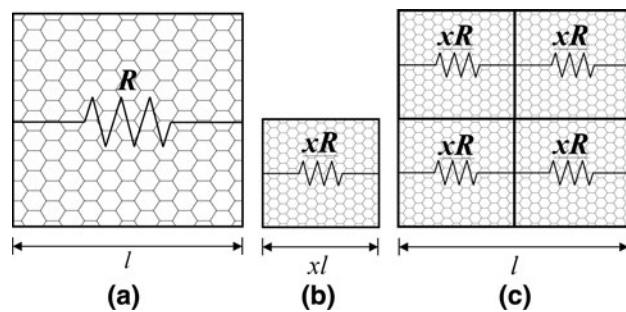


Fig. 1—Idealized microstructures: (a) initial microstructure, (b) initial microstructure scaled by factor x (0.5 as shown), and (c) scaled microstructure repeated to restore initial geometry.

preceding method. For the second case, $\mathbf{A}_x \mathbf{i}_x = \mathbf{b}_x$. Note that the first n rows of \mathbf{A}_x correspond to equations of the form $\sum_k a_{jk} i_{k,x} = 0$ for each node j and that they can be scaled by an arbitrary nonzero factor without affecting the solution of the matrix equation. The final $m-n$ rows of \mathbf{A}_x derive from equations $\sum_k c_{jk} R_{k,x} i_{k,x} = V^+$ that are related to the corresponding rows of \mathbf{A} by a factor of $R_k/R_{k,x} = 1/x$. Therefore, $\mathbf{A}_x = x\mathbf{A}$ and $\mathbf{b}_x = \mathbf{b}$, from which we obtain $\mathbf{i}_x = (1/x)\mathbf{i}$ and thus $R_{\text{eff},x}/R_{\text{eff},1} = x$.

In order to calculate the resistance per unit cross-sectional length for square images, the effective resistances in the regular hexagonal grid must be repeated $1/x$ times in the vertical and horizontal directions to fill the same space as the original network of unit length resistors (as shown in Figure 1(c)). This construction corresponds to a circuit with $1/x$ resistors in parallel, where each of those resistors corresponds to a series arrangement of resistors, each with resistance $R_{\text{eff},x} = xR_{\text{eff},1}$. The effective resistance of such a construction is given by Eq. [1]:

$$R_{\text{eff},\text{total}} = \left[\left(\frac{1}{2} \right) \frac{1}{x R_{\text{eff},1}} \right]^{-1} = x R_{\text{eff},1} \quad [1]$$

This equation shows that for a perfect hexagonal grid, altering the grain size by a factor of x will result in the effective resistance of a unit area also being multiplied by x . Therefore, to decouple the effect of grain size when comparing two samples, the effective resistance of the second sample can be multiplied by $(1/x)$, where x is the ratio of grain size between the two.

In the present analysis, because of the difficulties in selecting an appropriate grain size for a binary system of boundaries, the total HAB length ratio was used in place of the grain size ratio. The justification for considering only HABs in this case is that in a parallel system, it is the low-resistance boundaries that dominate the resistance of the network. For example, for the resistivity ratio $\rho_{(\Sigma 3n)}/\rho_{(\text{HAB})} = 12$, adding a similar $\Sigma 3$ boundary in parallel with an HAB will decrease the resistance of the system by ~ 7.7 pct. Adding a similar HAB instead will decrease the resistance of the system by 50 pct. It should be noted that for the analytical solution concerning a hexagonal grid, the HAB length ratio is linearly related to the grain size ratio and, hence, may be substituted.

The overall aim of the present study is to determine the effect of GBE on the microstructure of alloy 800H, a high-temperature single-phase alloy used commonly in the petrochemical industry. This alloy is employed at high temperatures (~ 0.7 melting point) and relatively low stresses. Future studies will investigate whether GBE has the potential to improve the creep performance of this alloy.

II. EXPERIMENTAL PROCEDURES

Material was obtained from Thyssenkrupp VDM Australia (Mulgrave, Victoria, Australia) in 4.5- and 8-mm sections of plate measuring 300×150 mm.

The nominal composition of 800H is 30 to 35 wt pct Ni, 19 to 23 wt pct Cr with a balance of iron and small additions of aluminum and titanium.^[23] The plate was cold machined into strips measuring 150 × 25 mm for rolling.

Each strip was then cold rolled using one of three different deformation percentages. Subsequent annealing was performed in a box furnace at one of three different temperatures and for 1 of 3 different times. This cycle was performed 4 times for each sample, with the same set of parameters (deformation percentage, annealing temperature, and annealing time). In this article, each individual process (deformation or annealing) is referred to as a step, and each combination of these two steps is referred to as a cycle.

Each processing parameter was assigned three relative states (low, medium, and high). For reasons of intellectual property ownership, the exact parameters cannot be reported, and hence, the GBE samples are identified using the labels S1 through S11. The remaining sample was not processed and, hence, represents the “as-received” condition, labeled as AR. The relationship between the labels and the processing parameters is shown in Table I.

Sections were cut from each of the samples with the surface of interest being a cross section perpendicular to the rolling direction. These sections were mounted using Buehler Probemet conductive molding compound and ground to a 600-grit finish using SiC pads. They were then polished to a 3- μm finish using diamond paste and finally electropolished using a 10 pct oxalic acid solution at 1.5 V for 12 seconds.

Orientation maps were obtained using EBSD for each sample using an HKL Channel 5 EBSD package (Oxford Instruments Abingdon, Oxfordshire, UK) coupled with a JEOL[†] JSM 6100 scanning electron micro-

data points, which were almost all in the grain boundaries. $\Sigma 3^n$ ($n \leq 3$) boundaries were identified using the Brandon criterion.^[24] For each map, the total boundary length fractions for $\Sigma 3$, $\Sigma 9$, and $\Sigma 27$ were calculated automatically using HKL software.

Grain size measurement was semiautomated, using the HKL software. Since each data point reflects a specific crystal orientation, grain boundaries are automatically determined as lines dividing groups of points of similar crystal orientation. Therefore, it is possible to detect every grain automatically and calculate statistics such as mean grain diameter. However, without user input, this method is prone to including some small “false” grains, often misindexed due to changes in pattern quality either near grain boundaries or occasionally within grains. In order to remove these false grains from the count, the initial average grain diameter was calculated, and then a filter was applied. A threshold value of 4 pct initial average area was employed and found to exclude most visually identified false grains, while including most small, true grains. The main advantages in using this semiautomated method over the optical methods described in ASTM E112 (Standard Methods for Determining Average Grain Size) are the increased accuracy and repeatability, and also the ability to automatically identify grain boundaries with specific misorientations (*i.e.*, twin boundaries), which is a significant part of this work.

There is evidence to support the inclusion of twin boundaries in grain size calculations (*e.g.*, Reference 25), on the basis that twins have an effect on the motion of dislocations. Therefore, both “twin-excluded” and “twin-included” grain sizes have been calculated for comparison in this study. The numbers given in Section III indicate the mean grain diameter based on equivalent circular grains.

The grain boundary connectivity was analyzed by considering a simplified model of two-dimensional grain boundary diffusion, as explained in Section I. The effective resistance to diffusion (of a specific unit area) was extracted from the analogous electric circuit, where grain boundary segments were each assigned a resistance based on their length and type. The effective resistance of each sample was normalized by its total HAB length to decouple the effect of changes in grain size and isolate the changes in boundary topology.

In order to investigate the microstructural evolution through GBE processing, two further samples were processed using the same parameters as S3 and S5. These samples were analyzed after each of five cycles to determine the changes in proportion of $\Sigma 3^n$ boundaries, grain size, and mean $\Sigma 3$ angular deviation. This mean $\Sigma 3$ angular deviation was calculated based on the raw orientation data from the HKL EBSD system. Each grain boundary segment (defined as a single section of boundary between two triple points) was assigned a single misorientation based on the difference between the mean grain orientation of each neighboring grain. The deviation from ideal, ν , was calculated by then comparing the boundary misorientation with the ideal $\Sigma 3$ misorientation using standard matrix multiplication methods.^[26] The low-angle boundary (LAB) fraction

[†]JEOL is a trademark of Japan Electron Optics Ltd., Tokyo.

scope. A total of 24 mm² was mapped for each sample at a step size of 10 μm . Typical successful pattern identification rates were between 95 and 98 pct. These maps were then processed using the HKL noise reduction algorithm to extrapolate the remaining unindexed

Table I. Relative Parameter States for Each Sample; Specific Conditions are Unable to be Reported

Sample	Deformation per Cycle	Annealing Temperature	Annealing Time
AR	—	—	—
S1	low	low	low
S2	low	low	med
S3	low	med	low
S4	low	med	med
S5	low	med	high
S6	low	high	low
S7	low	high	high
S8	med	med	med
S9	med	med	high
S10	high	med	low
S11	high	med	high

was also calculated within the HKL software, representing the length fraction of all grain boundaries with misorientations $2 \text{ deg} < \theta < 15 \text{ deg}$.

III. RESULTS AND DISCUSSION

This discussion is divided into four sections detailing the appearance of a typical GBE microstructure, the contribution to the GBE mechanism that the present work provides, the effects of variations in individual processing parameters, and the microstructural evaluation of GBE samples through connectivity analysis.

A. GBE Microstructure

Figure 2 shows a comparison between the as-received microstructure (AR) and a representative GBE microstructure (S3). Four images, highlighting $\Sigma 3$, $\Sigma 9$, $\Sigma 27$, and all $\Sigma 3^n$ ($n \leq 3$) boundaries, respectively, in black with general HABs in gray are presented.

These images are typical of GBE microstructures reported in the literature. After processing, there is a clear increase in the number fraction (and, correspondingly, the length fraction) of $\Sigma 3$ boundaries, accompanied also by increases in the relative length of $\Sigma 9$ and $\Sigma 27$ boundaries. These $\Sigma 9$ and $\Sigma 27$ boundaries are a result of the interactions between dissimilar $\Sigma 3$ boundaries and are geometrically constrained, where three $\Sigma 3^n$ boundaries meet at a triple junction.

B. Microstructural Evolution

In order to track the evolution of the microstructure throughout GBE processing, two samples (with the same processing parameters as S3 and S5) were analyzed

after each of five GBE processing cycles. These samples were subjected to identical deformation percentages and annealing temperatures, and therefore, their only difference is in annealing time. For convenience, these two samples are referred to in this section as “short annealed” and “long annealed.” The length fractions of $\Sigma 3^n$ boundaries were calculated after each GBE cycle, and the results are shown in Figure 3. A “diminishing return” trend in terms of total $\Sigma 3^n$ length fraction is observed for both samples. However, it is important to note that this trend actually begins at cycle 2. During the first cycle, the $\Sigma 3^n$ length fraction undergoes very little change, which indicates that, under these specific conditions, more than one step is necessary to achieve a GBE state. This statement is in general agreement with the majority of work in this field,^[12,20,27,28] although there are occasional instances of GBE states being reported after a single cycle. For example, Kokawa

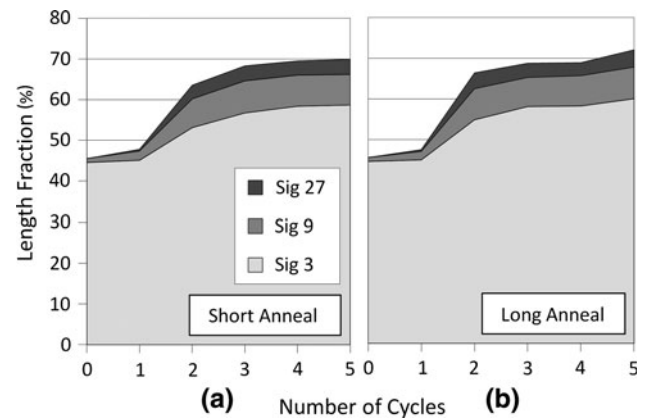


Fig. 3—Length fractions of $\Sigma 3^n$ boundaries for (a) short-annealed and (b) long-annealed samples after each of five GBE cycles.

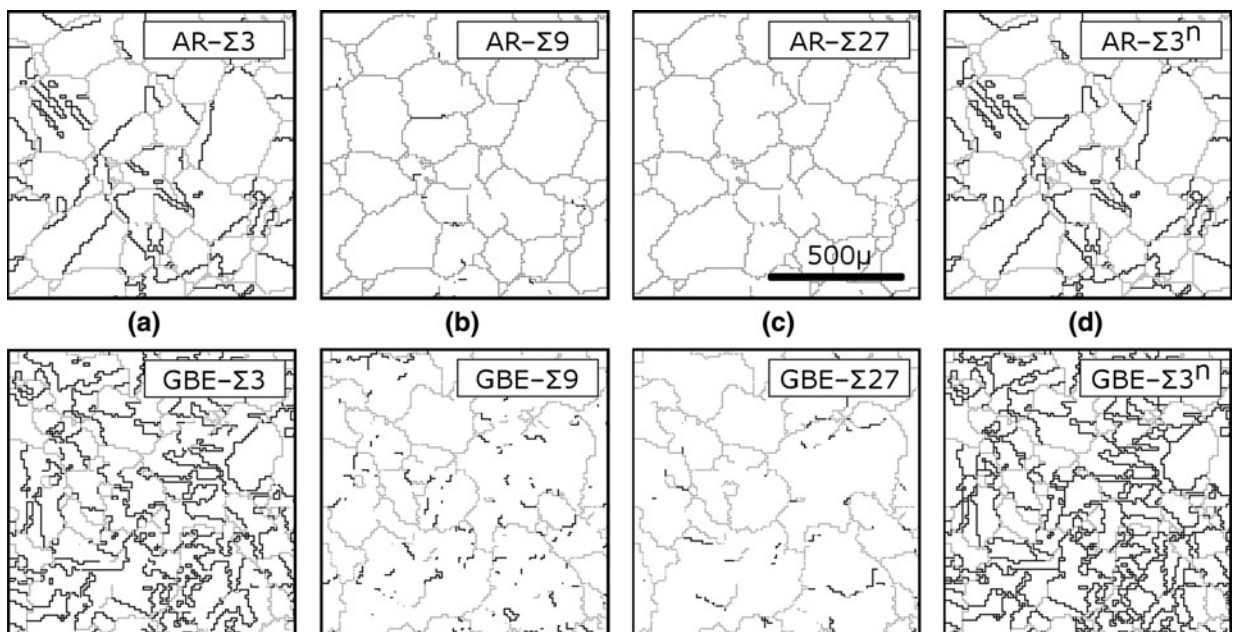


Fig. 2—Representative comparison between as-received (top) and GBE (bottom) conditions showing (a) $\Sigma 3$ boundaries; (b) $\Sigma 9$ boundaries; (c) $\Sigma 27$ boundaries; and (d) $\Sigma 3$, $\Sigma 9$, and $\Sigma 27$ boundaries highlighted in black. Gray lines indicate HABs.

et al.^[29] report very high length fractions of $\Sigma < 29$ boundaries in an austenitic 304 stainless steel after one cycle of 5 pct rolling and annealing at 1200 K to 1240 K (927 °C to 967 °C). Colman and Randle^[18] also showed that in copper a single GBE cycle increased the fraction of $\Sigma 3$ s, although these new $\Sigma 3$ s were mainly not incorporated into the GB network until subsequent processing cycles.

When $\Sigma 3^n$ fractions are reported as a function of processing cycle in the literature,^[30–32] the results generally show a somewhat erratic first or first few steps (the $\Sigma 3$ fraction may actually decrease slightly), followed by a general increase in the fraction of $\Sigma 3^n$ boundaries. In this present work, little effect was obtained from performing the first step, but subsequent processing steps resulted in increasing fractions of $\Sigma 3$, $\Sigma 9$, and $\Sigma 27$ boundaries.

The reasons for this trend are not well understood, although the issue has been addressed by Randle and Davies^[31] in a study of alpha-brass. They suggest that in the initial stages, the immobile twin boundaries provide strain retention. This is thought to be due mainly to the back stress generated from dislocation pileup at these boundaries. The retained strain is increased with the early deformation steps until it reaches a threshold level, at which point there is sufficient driving force for the mobile GB network to move through the structure, absorbing dislocations and hence removing the retained strain. During the next cycle, there is little retained strain. There is evidence of new twinning during these subsequent cycles, and the $\Sigma 3^n$ fraction increases. Owen and Randle go further in a study of 316 stainless steel.^[32] They suggest that the boundary migration is slower when the material has little retained strain (in the later cycles) and that this slower migration velocity is more suitable for the nucleation of annealing twins.

In the present work, it was desirable to determine whether the results supported the theories given in previous studies. The angular deviation from ideal misorientation provides important information about the energy of boundaries classified as $\Sigma 3$ in the network^[33] and the amount of retained strain in the grains on either side of these boundaries. The data are plotted as a weighted mean deviation parameter, \bar{v} , which is defined as follows:

$$\bar{v} = \frac{\sum_i^{\text{numof}\Sigma 3s} v_i L_i}{v_{\text{max}} \sum_i L_i} \quad [2]$$

where v_i = the angular deviation from ideal of $\Sigma 3$ boundary segment i , L_i = the length of $\Sigma 3$ boundary segment i , and v_{max} = the maximum allowable deviation from the Brandon criterion (~8.7 deg).

The weighted mean deviation parameter for both samples is shown in Figure 4. The LAB fraction is a separate indicator of retained strain in the lattice and is also included in Figure 4. In this figure, points are joined as a guide only.

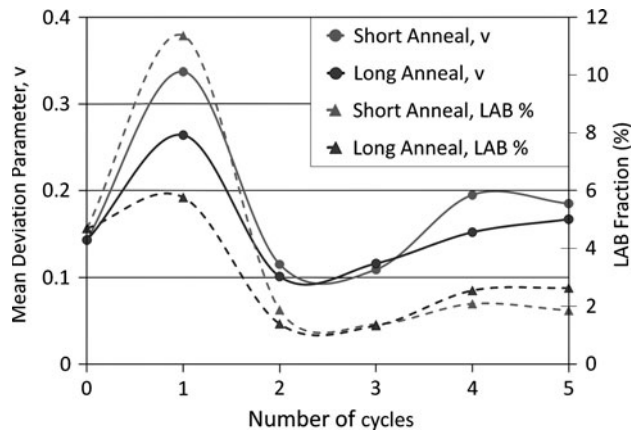


Fig. 4—Mean $\Sigma 3$ deviation parameter (\bar{v}) and LAB fraction for short-annealed and long-annealed samples after each of five GBE cycles.

Figure 4 shows that the mean $\Sigma 3$ angular deviation increases significantly after the first processing cycle. This trend is present for both samples, although the increase is greater for the short-annealed sample. The same result was obtained in a previous study of this material,^[34] where the $\Sigma 3$ deviation was then found to decrease with increasing annealing time up to 90 minutes after one deformation step. In both cases, the increase in $\Sigma 3$ deviation is likely due to the effect of dislocation pileup in the neighboring lattices. Correspondingly, the LAB fraction increases from 4.7 to 11.4 pct for the short-annealed sample and to 5.8 pct for the long-annealed sample. These results show that the first processing cycle served to increase the overall amount of retained strain in the material. It follows that the annealing conditions were not sufficient in either case to remove the deformation introduced during the rolling step, although the long-anneal step should lead to lower retained strain levels. After the second cycle, however, the mean $\Sigma 3$ deviation parameter decreased to a level below that of the as-received material in both samples. Similarly, the LAB fractions decreased to levels approximately one-third of the as-received condition. These results indicate that a significant proportion of the retained strain that was present in the material after one cycle was removed by the second cycle. Certainly, migration of mobile boundaries and dislocation absorption could explain this result. The simplest evidence for boundary migration is the change in grain size for both samples, as plotted in Figure 5.

The trend in grain size reflects that of the $\Sigma 3^n$ fraction, in that it remains constant for the first cycle before increasing significantly during the second. Less significant increases are also observed in the subsequent cycles. This analysis, therefore, provides evidence of boundary migration through cycles 2 to 5, which is probably most significant during cycle 2. Smaller increases in $\Sigma 3^n$ fraction and retained strain levels are also noticed during these later cycles.

In summary, both the short-annealed sample and the long-annealed sample exhibited similar trends during GBE processing. During cycle 1, levels of retained strain

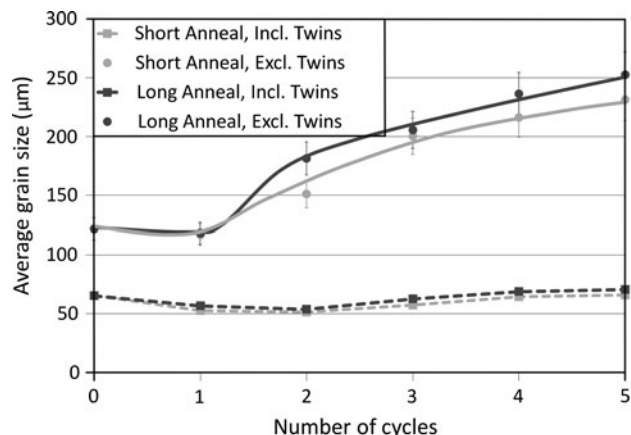


Fig. 5—Grain sizes (including and excluding twin boundaries) of short-annealed and long-annealed samples after each of five GBE cycles. Error bars show standard deviation from each set of 24 images.

increased, the $\Sigma 3''$ fraction remained relatively unchanged, and the grain size remained constant, suggesting little boundary migration. During cycle 2, levels of retained strain decreased significantly to levels below those of the as-received condition. $\Sigma 3''$ fraction and grain size showed their largest increases for all cycles after cycle 2. In cycles 3 through 5, small increases were observed in retained strain levels, grain size, and $\Sigma 3''$ fraction.

These results are consistent with the mechanisms discussed previously in the literature. The largest increases in $\Sigma 3$ fraction were observed in both (a) the same cycle as the largest decrease in $\Sigma 3$ deviation parameter (as in the present study, and also Reference 31) and (b) the cycle immediately following the largest decrease in $\Sigma 3$ deviation parameter.^[32] With regard to the theory that low retained strain levels (and, hence, relatively slow boundary migration) are more suitable for the generation of annealing twins, as suggested for case (b), it is still possible that the absorption of retained strain (relatively high boundary velocity) and the $\Sigma 3$ generation occur consecutively within the same annealing step, which would be consistent with case (a). The fact that the as-received condition contained few $\Sigma 9$ and $\Sigma 27$ boundaries after its manufacturing process of heavy deformation and high-temperature annealing would suggest that extremely high boundary velocities are not suitable for creating a GBE state.

C. Effects of Processing Parameters

The length fractions of $\Sigma 3''$ boundaries were calculated for all 11 GBE samples representing different combinations of the three GBE parameters. These results are shown in Figure 6. The as-received sample (AR) contains boundary length fractions of approximately 42 pct for $\Sigma 3$, ~1 pct for $\Sigma 9$, and ~0 pct for $\Sigma 27$. The lack of the $\Sigma 3$ geometric counterparts ($\Sigma 9$ and $\Sigma 27$) shows that the material is not in a GBE state. The results show that all combinations of GBE parameters resulted in increases in the length fraction of $\Sigma 3''$

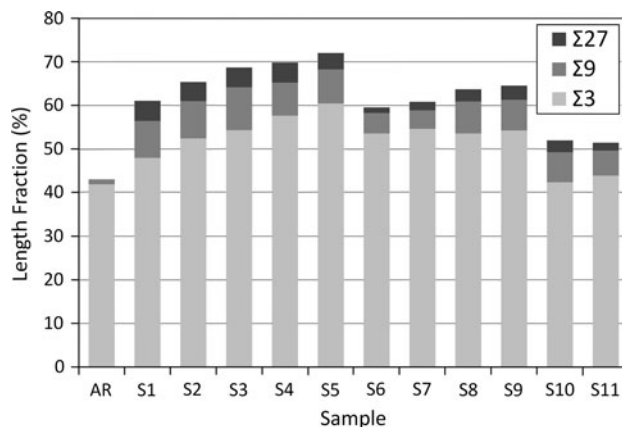


Fig. 6—Length fractions of $\Sigma 3''$ boundaries for all GBE samples.

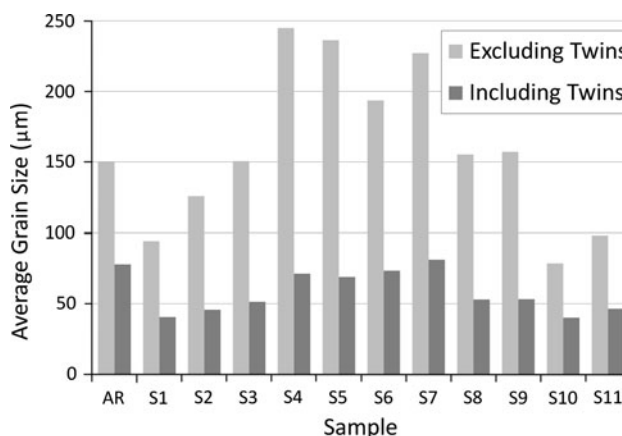


Fig. 7—Grain sizes, including and excluding twins for all GBE samples.

boundaries, as compared to the as-received sample. Specifically, the increases in $\Sigma 9$ and $\Sigma 27$ fractions show that some amount of GBE has taken place in all 11 processed samples.

The average grain size was also calculated for each sample (both excluding twins and including twins as grain boundaries) and the results are shown in Figure 7. In the majority of cases, the GBE process has caused the ratio between the twin-excluded grain size and the twin-included grain size to change. For example, this ratio is ~2 in the AR sample and shows increases up to ~3.5 in the GBE samples. This is obviously consistent with the introduction of new twins.

As one of the aims of this work was to optimize the GBE conditions with respect to $\Sigma 3''$ fraction as well as grain size, the local effect of variation in each GBE parameter is briefly discussed in turn.

1. Deformation percentage

The effect of deformation percentage can be seen when comparing samples S5, S9, and S11. These samples have all been annealed under the same conditions and represent the three states of deformation (low, medium, and high). Figure 3 shows that increasing the deformation percentage within this range causes the

length fraction of $\Sigma 3^n$ boundaries to decrease relative to S5. This general trend is also noticeable when considering the entire range of the samples, in that the low-deformation samples (S1-S7) generally show higher $\Sigma 3^n$ fractions than the medium (S8-S9) or high-deformation (S10-S11) samples. In terms of grain size, Figure 4 shows that, for the same samples (S5, S9, and S11), the grain size decreases with increasing deformation.

2. Annealing temperature

The effect of annealing temperature can be isolated by considering samples S1, S3, and S6, representing low deformation, low annealing time, and low, medium, and high annealing temperatures, respectively. Figure 6 shows that there is a local maximum in the $\Sigma 3^n$ fraction in between T_{low} and T_{high} , indicating that there is a local intermediate temperature that will yield the greatest return in terms of $\Sigma 3^n$ fraction. Figure 7 shows the expected trend of increasing grain size with increasing annealing temperature over these three samples.

3. Annealing time

The effect of annealing time is isolated by considering samples S3, S4, and S5, representing low deformation, intermediate annealing temperature, and low, medium, and high annealing times, respectively. In these three samples, $\Sigma 3^n$ fraction is seen to increase slightly with increasing annealing time. This result is also noticeable in the other conditions (*e.g.*, S1 and S2). Figure 7 again shows the expected trend of increasing grain size with increasing annealing time for most conditions, although S4 is slightly anomalous compared to S3 and S5.

4. Summary of GBE parameters

Although the actual parameters used in these experiments cannot be reported, it is important to note that alloy 800H appears to have a certain combination of GBE parameters within the range tested, which results in a local maximum in boundary length fraction of $\Sigma 3$, $\Sigma 9$, and $\Sigma 27$ boundaries. Small deviations from these parameters have been shown to still result in GBE, but with reduced $\Sigma 3^n$ fractions compared to this maximum. Hence, it is likely that for many examples of GBE presented in the literature, small alterations in the relevant parameters may increase the $\Sigma 3^n$ boundary fraction, possibly leading to a more optimized microstructure. The reasons for this are obviously linked to the GBE mechanism, which is still under research, although the amount of retained strain in the material and the migration speed of mobile boundaries have been suggested as important.^[32] Retained strain is built up during the deformation steps and provides the driving force for boundary migration. If the retained strain is insufficient for boundary migration, GBE likely cannot occur. If the retained strain is too high, special boundaries may be destroyed by the introduction of dislocations and may not necessarily revert to their original geometry. It has also been proposed previously that boundary velocity may be too high to support new twin generation. In the present work, it was found that of the three deformation percentages, the “low” state was most successful in increasing $\Sigma 3^n$ length fraction, and

therefore, it follows that boundary migration occurred in all samples. The annealing temperature obviously also influences boundary migration speed, and it follows that annealing conditions could also be insufficient for migration or too high for new twin generation. In fact, at least one study^[35] has been published in the literature where the $\Sigma 3^n$ boundary fraction was slightly decreased by attempted GBE processing. Therefore, if the specific aim of a GBE procedure is to optimize the fraction of $\Sigma 3^n$ CSL boundaries, it is recommended that a range of conditions is first tested and then refined surrounding those that seem to be optimal.

IV. MICROSTRUCTURAL EVALUATION

While the length fraction of low- Σ CSL boundaries is used in this case as a measure of how “engineered” the material is, it should not be used as a predictor of material properties. Instead, this information should be combined with other information such as an indication of the boundary planes (where possible) and a knowledge of the likely damage mechanisms. Some damage mechanisms such as stress corrosion or Coble creep (grain boundary diffusion-based creep) rely on the grain boundary network as a transport network. One major way in which GBE is thought to resist such mechanisms is by breaking up the interconnected HAB network and, therefore, reducing its transport properties. In fact, there has been some work published regarding the influence of boundaries with special properties and their effect on theoretical GB transport networks (*e.g.*, References 36 and 37). However, the measurement of such disruption has not been standardized. A common method of measuring the connectivity of the HAB network is to analyze all of the triple points and classify each based on the number of special (usually $\Sigma < 29$) boundaries it joins. However, a situation where multiple twins and twin variants meet inside a single grain will certainly increase this fraction, but will likely offer no disruption to the transport network provided the original HABs remain. Therefore, a more direct measurement of grain boundary connectivity is needed.

In the present work, this disruption of the HAB network can be shown in two ways. Figure 8 shows sample HAB networks from 2 of the 12 samples (AR and S5). These images have been processed by removing

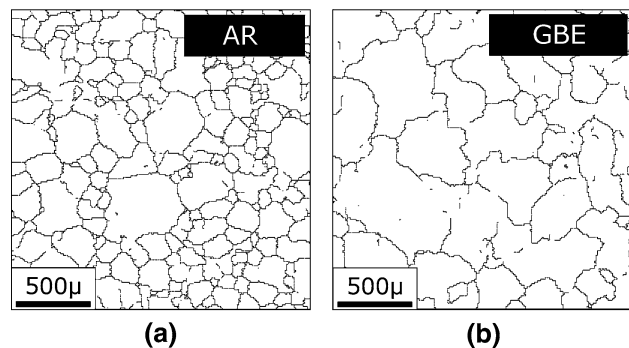


Fig. 8—HAB networks of (a) AR and (b) S5 (highest $\Sigma 3^n$ fraction).

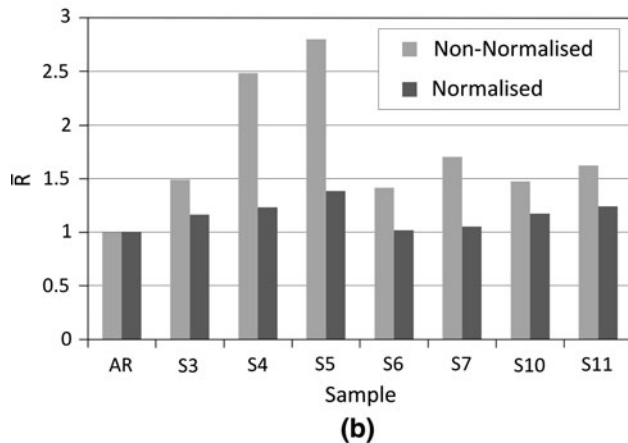
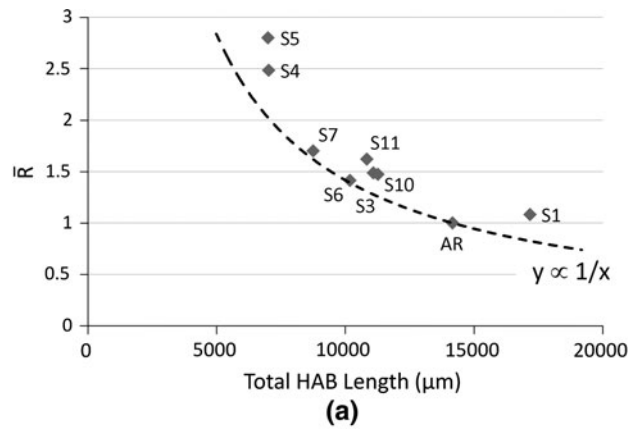


Fig. 9—(a) Correlation between \bar{R} and total HAB length for selected samples, showing the analytical solution for microstructural scaling effects. (b) \bar{R} for selected GBE conditions, normalized against total HAB length.

the $\Sigma 3^n$ family. Visual comparison with the as-received sample shows qualitatively that the connectivity of the HAB network has been interrupted through the inclusion of these extra $\Sigma 3^n$ boundaries in the GBE sample.

Figure 9 shows the results of the grain boundary network connectivity analysis, explained in Section I. This analysis was performed by converting each EBSD map to a network of resistors where each grain boundary segment was assigned a resistance value based on its length and boundary type. The two-dimensional effective resistance, R_{eff} , of the network was then found by solving the analogous electric circuit problem. Plotted are the ratios between the R_{eff} value for each sample and the R_{eff} value for the as-received sample. This ratio is denoted \bar{R} .

Figure 9(a) shows \bar{R} for each sample, as a function of total HAB length. The dotted line in this figure indicates the \bar{R} values that would result solely from changes in grain size according to the derived relationship $\bar{R} \propto (1/x)$. It is apparent that the majority of the GBE data lie well above this line, signifying that there is a definite change in boundary topology, which acts in addition to the change in boundary length. This is confirmed in Figure 9(b), showing both the raw and normalized \bar{R} for each sample. These figures show that all of the GBE samples exhibited some increase in

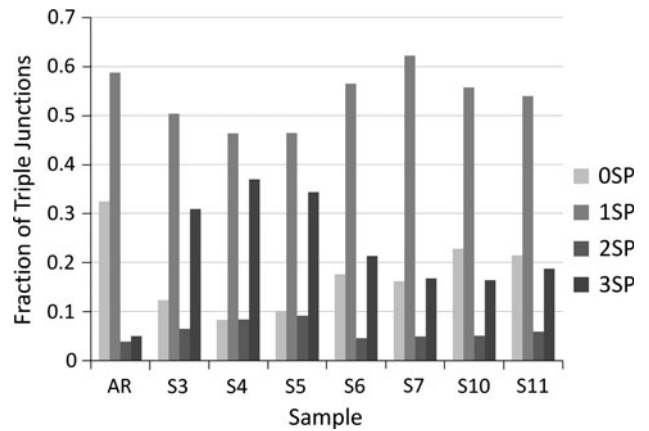


Fig. 10—Fraction of triple junctions joining zero, one, two, and three $\Sigma 3^n$ boundaries (0-3SP) for as-received and selected GBE samples.

effective resistance, with the greatest disruption to the HAB network occurring in samples S4 and S5. These are also the samples with the highest $\Sigma 3^n$ fractions (Figure 6). It should also be noted that this difference would be compounded in the real, three-dimensional case. These results show that the high-temperature annealed samples (S6 and S7) exhibit increases in $\Sigma 3^n$ boundary fraction of ~40 pct, but only a very small increase in normalized effective resistance. This is consistent with twin and twin variants being introduced internally within the existing HAB structure, which will not effectively disrupt the existing HAB network and may not reduce grain boundary transport properties compared to an as-received sample with a similar grain size.

As the present analysis has not been previously published in the literature, a triple junction analysis is also presented in order to provide some continuity with existing studies. Figure 10 shows the relative fraction of triple junctions joining 0, 1, 2, and 3 special ($\Sigma 3^n$) boundaries for each sample (0 to 3 SP).

Similar trends are seen when the triple junction analysis results are considered. Figure 10 shows that 32 pct of the triple junctions in the as-received sample join only HABs, and approximately 5 pct join three $\Sigma 3^n$ boundaries. In the highest $\Sigma 3^n$ fraction samples (S4 and S5), the number of HAB-only triple junctions drops to 10 to 12 pct and the number of $\Sigma 3^n$ -only triple junctions is increased to 34 to 37 pct. For these samples, the $\Sigma 3^n$ -only fraction is predominantly made up of the $\Sigma 3$ - $\Sigma 3$ - $\Sigma 9$ (~66 pct) and $\Sigma 3$ - $\Sigma 9$ - $\Sigma 27$ (~33 pct) junctions. When the high-temperature annealed samples are considered (S6 and S7), similar trends are observed, but to a lesser extent than samples S4 and S5. In this case, the $\Sigma 3^n$ -only fraction is made up of the same two junctions ($\Sigma 3$ - $\Sigma 3$ - $\Sigma 9$ and $\Sigma 3$ - $\Sigma 9$ - $\Sigma 27$) but in the ratio ~73 to ~27 pct. This shows that fewer multiple twinning operations have taken place compared to S4 and S5, which is consistent with the lower $\Sigma 9$ and $\Sigma 27$ fractions from Figure 6. Importantly, however, these results could be misinterpreted as a significant disruption to the HAB network when compared to the as-received triple junction fractions. The present analysis has shown that this is likely

not the case for these samples. Despite this disagreement, in general, there is reasonable correlation between the triple junction analysis and the connectivity model used in this work. Both analyses suggest that the greatest disruption to the HAB network occurs in samples S4 and S5, which also exhibit the highest $\Sigma 3^n$ fractions.

V. SUMMARY AND CONCLUSIONS

A microstructural study of 11 grain boundary engineered samples of alloy 800H was performed using EBSD. Each sample received a different GBE treatment, as defined by a matrix of GBE parameters (rolling deformation percentage, annealing temperature, and annealing time). The relative length fraction of $\Sigma 3^n$ CSL boundaries was increased in all cases; thus, it can be concluded that there is a variety of parameter combinations that will create a GBE material. The maximum $\Sigma 3^n$ length fraction of 72.1 pct was attained using a relatively low deformation level and an intermediate annealing temperature (the specific conditions are unable to be reported due to confidentiality). Annealing time had only a small effect under these conditions. The maximum attained $\Sigma 3^n$ fraction represents a 70 pct increase over the as-received sample.

Two samples were subjected to a further study, involving characterization after each of five total GBE cycles. For both samples, the $\Sigma 3^n$ fraction was shown to remain unchanged during the first cycle, before increasing through the next four. Retained strain levels (as measured by $\Sigma 3$ deviation and LAB fraction) were shown to increase during this first cycle, before decreasing sharply during the second. These results are consistent with other such analyses published in the literature and add support to these studies.

A boundary connectivity analysis method was developed to measure the extent of $\Sigma 3^n$ incorporation into the GB network by means of a simplified two-dimensional diffusion model. All GBE samples exhibited some extent of $\Sigma 3^n$ incorporation, shown by increases in two-dimensional diffusion resistance; however, the highest levels of incorporation were consistent with the highest $\Sigma 3^n$ length fractions. These results were also consistent with an analysis of the triple junctions for each sample, which is a common method of analyzing boundary connectivity found in the literature. A study of secondary creep rate in these GBE conditions is in progress and is expected to show some correlation with the effective resistance results. The results of this study will be reported at a later date.

ACKNOWLEDGMENTS

The authors acknowledge the continued generous support of Methanex New Zealand, Schmidt and Clemens (S.A.), and Tubacex (S.A.), as well as the financial support of the New Zealand Tertiary

Education Commission (TEC) through a TEC Enterprise grant (Contract No. UOCX05014).

REFERENCES

1. T. Watanabe: *Res. Mech.*, 1984, vol. 11, pp. 47–84.
2. V. Randle: *Mater. Sci. Technol.*, 2010, vol. 26, pp. 253–61.
3. P. Lin, G. Palumbo, U. Erb, and K.T. Aust: *Scripta Metall. Mater.*, 1995, vol. 33, pp. 1387–92.
4. E.M. Lehockey, A.M. Brennenstuhl, and I. Thompson: *Corros. Sci.*, 2004, vol. 46, pp. 2383–2404.
5. V. Thaveerungsriporn and G.S. Was: *Metall. Mater. Trans. A*, 1997, vol. 28A, pp. 2101–12.
6. T. Watanabe and S. Tsurekawa: *Acta Mater.*, 1999, vol. 47, pp. 4171–85.
7. E.M. Lehockey, G. Palumbo, and P. Lin: *Metall. Mater. Trans. A*, 1998, vol. 29A, pp. 3069–79.
8. S.M. Schlegel, S. Hopkins, and M. Frary: *Scripta Mater.*, 2009, vol. 61, pp. 88–91.
9. L.S. Shvindlerman and B.B. Straumal: *Acta Metall.*, 1985, vol. 33, pp. 1735–49.
10. V. Randle: *Mater. Sci. Technol.*, 1999, vol. 15, pp. 246–52.
11. V. Randle: *Scripta Mater.*, 2001, vol. 44, pp. 2789–94.
12. M. Kumar, W.E. King, and A.J. Schwartz: *Acta Mater.*, 2000, vol. 48, pp. 2081–91.
13. V. Randle: *Acta Mater.*, 1997, vol. 46, pp. 1459–80.
14. K.L. Merkle and D. Wolf: *Philos. Mag. A*, 1992, vol. 65, pp. 513–30.
15. G.S. Rohrer, D.M. Saylor, B.S. El-Dasher, B.L. Adams, A.D. Rollett, and P. Wynblatt: *Z. Metallkd.*, 2004, vol. 95, pp. 197–214.
16. T. Skidmore, R.G. Buchheit, and M.C. Juhas: *Scripta Mater.*, 2004, vol. 50, pp. 873–77.
17. X. Fang, W. Wang, H. Guo, X. Zhang, and B. Zhou: *J. Iron Steel Res. Int.*, 2007, vol. 14 (5), pp. 339–43.
18. M. Coleman and V. Randle: *Metall. Mater. Trans. A*, 2008, vol. 39A, pp. 2175–83.
19. C.A. Schuh, M. Kumar, and W.E. King: *Acta Mater.*, 2003, vol. 51, pp. 687–700.
20. Y. Gao, J.S. Stölken, M. Kumar, and R.O. Ritchie: *Acta Mater.*, 2007, vol. 55, pp. 3155–67.
21. Y. Chen and C.A. Schuh: *Acta Mater.*, 2006, vol. 54, pp. 4709–20.
22. B. Alexandreanu, B.H. Sencer, V. Thaveerungsriporn, and G.S. Was: *Acta Mater.*, 2003, vol. 51, pp. 3831–48.
23. *Special Metals Technical Bulletin SMC-047—“Incoloy 800H and 800HT,”* available at www.specialmetals.com.
24. D.G. Brandon: *Acta Metall.*, 1966, vol. 14, pp. 1479–84.
25. L. Lu, Y. Shen, X. Chen, L. Qian, and K. Lu: *Science*, 2004, vol. 304, pp. 422–26.
26. V. Randle: *The Measurement of Grain Boundary Geometry*, IOP Publishing Ltd., Bristol, UK, 1993.
27. V. Thaveerungsriporn, P. Sinsrok, and D. Thong-Aram: *Scripta Mater.*, 2001, vol. 44, pp. 67–71.
28. U. Krupp, W.M. Kane, X. Liu, O. Dueber, C. Laird, and C.J. McMahon: *Mater. Sci. Eng. A*, 2003, vol. 349, pp. 213–17.
29. H. Kokawa, M. Shimada, M. Michiuchi, Z.J. Wang, and Y.S. Sato: *Acta Mater.*, 2007, vol. 55, pp. 5401–07.
30. W.E. King and A.J. Schwartz: *Scripta Mater.*, 1998, vol. 38, pp. 449–55.
31. V. Randle and H. Davies: *Metall. Mater. Trans. A*, 2002, vol. 33A, pp. 1853–57.
32. G. Owen and V. Randle: *Scripta Mater.*, 2006, vol. 55, pp. 959–62.
33. J. Furley and V. Randle: *J. Mater. Sci. Technol.*, 1991, vol. 7, pp. 12–19.
34. L. Tan and T.R. Allen: *Metall. Mater. Trans. A*, 2005, vol. 36A, pp. 1921–25.
35. C.J. Boehlert: *Mater. Sci. Eng. A*, 2008, vol. 473, pp. 233–37.
36. W.S. Tong, J.M. Rickman, H.M. Chan, and M.P. Harmer: *J. Mater. Res.*, 2002, vol. 17, pp. 348–52.
37. Y. Chen and C.A. Schuh: *Phys. Rev. B*, 2007, vol. 76 (6), article no. 064111, pp. 1–12.